https://doi.org/10.58225/sw.2026.1-125-131

# CORRELATION BETWEEN STRUCTURAL STABILITY, OXIDATION BEHAVIOR AND LATTICE DYNAMICS IN GAMMA-IRRADIATED TiN NANOPARTICLES

Alena V. Shershneva[1*], Mahmoud Ibrahim[1,2]
[1]*Tomsk Polytechnic University, Tomsk 634050, Russia.*
[2]*Joint Institute for Nuclear Research, Dubna 141980, Russia*
**avs322@tpu.ru*

**Abstract.** This study presents an integrated assessment of the crystal structure, post-irradiation oxidation behavior and vibrational response of titanium nitride (TiN) nanoparticles exposed to gamma radiation. Nanopowders with an average particle size below 20 nm were irradiated using a $^{60}$Co source at absorbed doses of 50, 200, 900 and 3500 kGy. Structural changes after annealing at 1173 K were examined by X-ray diffraction and Rietveld refinement, while dose-dependent lattice dynamics were evaluated by Raman spectroscopy in the 100–600 cm$^{-1}$ range. The cubic Fm-3m structure remained stable throughout irradiation, and no radiation-induced phase transformation was detected. After annealing, rutile $TiO_2$ was identified as a minor phase; its fraction decreased from 6.40 % in the unirradiated specimen to 3.88% after irradiation at 3500 kGy. High-dose irradiation followed by annealing reduced microstrain and dislocation density and increased the average crystallite size to approximately 50 nm. Four Raman modes near 152, 246, 359 and 500 cm$^{-1}$ persisted at every dose, although their positions, widths and areas changed. The combined results show that gamma irradiation does not destabilize the TiN framework but modifies defects, interatomic distances and surface-bound species, thereby suppressing subsequent oxidation and altering the vibrational response.

**Keywords:** TiN nanoparticles, gamma irradiation, Rietveld refinement, oxidation, Raman spectroscopy, lattice dynamics

***Cite this article as:*** *A. V. Shershneva and M. Ibrahim, "CORRELATION BETWEEN STRUCTURAL STABILITY, OXIDATION BEHAVIOR AND LATTICE DYNAMICS IN GAMMA-IRRADIATED TiN NANOPARTICLES",* SW AzUAC, *vol. 1, 2026, https://doi.org/10.58225/sw.2026.1-125-131*
***Article history:*** *Received: 25 May 2026 / Revised: 3 June 2026 / Accepted: 04 July 2026*

**1. Introduction**. Titanium nitride is a refractory ceramic combining a high melting point, high hardness, electrical conductivity and resistance to chemical degradation. These properties support its use in nuclear systems, protective coatings, diffusion barriers, plasmonic devices and components exposed to aggressive thermal environments [1–3]. Its mechanical, corrosion-resistant and electronic characteristics further broaden the range of potential applications. TiN nanoparticles have also attracted interest as near-infrared photothermal and plasmonic agents [4]. At the nanoscale, however, the large surface-to-volume ratio increases the contribution of adsorbed oxygen, water and structural defects; consequently, irradiation and heating may affect nanopowders differently from bulk TiN.

Energetic particles can produce vacancies, interstitials, residual stress and symmetry-lowering distortions in TiN. Ar-ion irradiation has been associated with lattice expansion and dislocation formation, whereas Xe implantation caused peak splitting, lattice contraction and rhombohedral distortion in thin films [5]. Electron irradiation likewise modifies the structural and functional response of TiN films [6]. These observations show that the response depends on particle type, energy, fluence and specimen morphology. Gamma photons mainly interact through electronic excitation and secondary electrons, so their crystallographic consequences can be subtler than those caused by direct ion displacement [7].

Temperature introduces an additional mechanism because TiN surfaces oxidize when oxygen becomes sufficiently mobile. Rutile $TiO_2$ develops during heating, and oxidation progresses from the surface toward the interior with nitrogen release [8]. The thermal behavior is also affected by particle size, surface chemistry and irradiation history [9]. Gamma irradiation may modify oxidation by removing weakly bound surface species, generating defects and changing diffusion paths. Earlier diffraction work demonstrated that nanocrystalline TiN retains its cubic phase up to 3500 kGy, although small contractions of the unit cell occur. Post-irradiation annealing further changes phase fractions, crystallite size and microstrain [10].

Diffraction provides information on long-range order and phase composition, whereas Raman spectroscopy probes local bonding, phonon behavior and disorder. Raman measurements are therefore valuable for identifying irradiation-induced changes that do not produce a new crystallographic phase [10-17]. Vibrational spectroscopy has been successfully used to connect local structural rearrangement with macroscopic stability in a wide range of crystalline systems [18].

The present work correlates XRD/Rietveld observations after irradiation and annealing with the dose-dependent Raman response of TiN nanoparticles. The objective is to determine whether the preserved average crystal symmetry is accompanied by local vibrational and defect evolution, and to clarify how prior gamma exposure influences subsequent oxidation.

**2. Materials and Methods**. Commercial TiN nanopowder supplied by US Research Nanomaterials, Inc. was used. The purity was 99.2%, the particle size was below 20 nm, the specific surface area was 50–80 $m^2$ $g^{-1}$, the bulk density was 0.08 g cm−3 and the true density was approximately 5.24 g $cm^{-3}$. TiN has a face-centered cubic structure described by space group Fm-3m [11,12].

Irradiation was conducted in air at room temperature using a 60Co gamma source at the Institute of Radiation Problems. Absorbed doses were 50, 200, 900 and 3500 kGy. The irradiation conditions and facility characteristics are described in [10]. For the thermal series, each irradiated powder and an unirradiated reference were annealed at 1173 K for 9 h under a vacuum of about $10^{-6}$ Torr; heating and cooling rates were 5 °C $min^{-1}$.

XRD patterns were recorded at room temperature with a PANalytical EMPYREAN diffractometer using Cu Kα radiation (λ = 1.5405 Å) in θ/2θ geometry. The angular interval was 20–100°, with a 0.02° step. Rietveld refinement was carried out with the FullProf suite. Phase fractions, lattice parameters and fit indices were refined. Crystallite size and microstrain were estimated from line broadening by the Williamson–Hall approach.

Raman spectra were collected at room temperature with a Horiba LabRAM HR spectrometer using a 633 nm He–Ne laser, an 1800 groove mm−1 grating, a 100 μm confocal aperture and a 50× objective. Laser power was 0.5 mW. Spectra were acquired for 30 s over ten accumulations, and five measurements were averaged per specimen. The 100–600 cm−1 spectra were fitted with mixed Lorentzian–Gaussian components.

**3. Results and Discussion**

**3.1. Crystal structure after gamma irradiation and annealing**. Figure 1 presents the Rietveld-refined diffraction patterns of the initial TiN powder and the specimens annealed at 1173 K after irradiation at different doses. The annealed diffraction patterns are dominated by reflections of cubic TiN. Rietveld analysis confirms space group Fm-3m for all specimens. Weak reflections at approximately 54.33° and 56.63°, assigned to the (211) and (220) planes of tetragonal rutile $TiO_2$ (P42/mnm), reveal limited oxidation during annealing. No other crystalline products were detected.

The oxide fraction decreases systematically as the preceding gamma dose rises: 6.40% for the unirradiated sample, 5.16% at 50 kGy, 5.10% at 200 kGy, 4.00% at 900 kGy and 3.88% at 3500 kGy. Thus, irradiation does not itself generate a detectable bulk oxide phase; instead, it weakens the subsequent oxidation response. A plausible explanation is the radiation-induced decomposition and desorption of surface-bound water and oxygen-bearing species, accompanied by defect rearrangement and partial structural compaction [19].

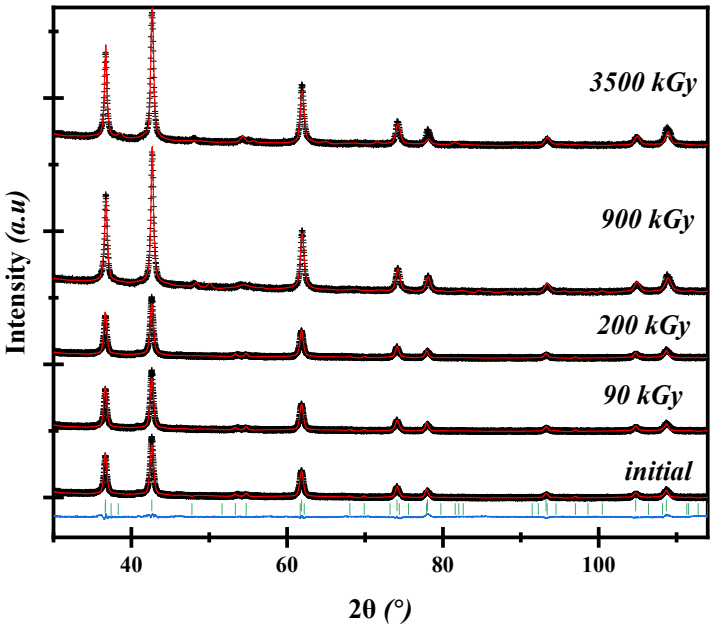


**Fig.1.** Rietveld-refined XRD patterns of TiN nanoparticles irradiated at different gamma doses and annealed at 1173 K

The principal (111) and (200) reflections retain their positions and overall profiles, confirming the stability of the cubic TiN phase. Their intensities and breadths nevertheless change with irradiation dose. After irradiation at 900 and 3500 kGy followed by annealing, the reflections become more intense, indicating improved crystalline ordering. The residual line broadening shows that irradiation-induced stress and defects are not completely removed. The refined lattice parameter varies only slightly around 4.24 Å, while the unit-cell volume remains within 76.1–76.3 $Å^3$.

The structural parameters summarized in Table 1 show that annealing increases the average crystallite size from the nominal 20 nm powder value to 43.5 nm in the unirradiated reference. Values of 42.1, 42.6, 50.0 and 49.9 nm were obtained after 50, 200, 900 and 3500 kGy, respectively. Microstrain decreases from $26.65\times10^{-4}$ to $25.78\times10^{-4}$, while the calculated dislocation-density indicator falls from $2.04\times10^{-6}$ to $1.72\times10^{-6}$ at the maximum dose. These changes indicate thermally assisted defect recombination and crystallite coarsening, most pronounced after high-dose exposure.

**Table 1.** Principal structural parameters of annealed TiN specimens

| Dose | a (Å) | V ($Å^3$) | Crystallite size (nm) | Microstrain ($\times10^{-4}$) |
|---|---|---|---|---|
| Initial | 4.2400 | 76.230 | 43.5 | 26.65 |
| 50 kGy | 4.2369 | 76.060 | 42.1 | 25.50 |
| 200 kGy | 4.2360 | 76.060 | 42.6 | 25.30 |
| 900 kGy | 4.2404 | 76.246 | 50.0 | 25.97 |
| 3500 kGy | 4.2410 | 76.287 | 49.9 | 25.78 |

The diffraction-line broadening was further evaluated by the Williamson–Hall (W–H) method [20]. The measured FWHM values were corrected for instrumental broadening using the $LaB_6$ standard and analyzed with the uniform-deformation relation:

$$\beta\cos\theta = \frac{k\lambda}{D} + 4\varepsilon\sin\theta \qquad (1)$$

Here, β is the instrument-corrected peak broadening expressed in radians, θ is the Bragg angle, k is the shape factor (0.9), λ is the Cu Kα wavelength (1.5405 Å), D is the volume-weighted average crystallite size, and ε is the microstrain. In the conventional W–H representation, β cos θ is plotted against 4 sin θ; the intercept equals kλ/D and the slope gives ε. Figure 2 displays the FWHM input points as a function of 2θ, while the values of D and ε were obtained after applying the W–H transformation in Eq. (1).

The W–H results are consistent with the values summarized in Table 1. The average crystallite sizes are 43.5 nm for the annealed initial sample and 42.1, 42.6, 50.0, and 49.9 nm for the samples irradiated at 50, 200, 900, and 3500 kGy, respectively, before annealing. Thus, the low-dose specimens remain close to 42 nm, whereas irradiation at 900 and 3500 kGy followed by annealing produces crystallites of about 50 nm. The corresponding microstrain values are 26.65, 25.50, 25.30, 25.97, and 25.78 × $10^{-4}$. The lowest microstrain is obtained at 200 kGy; all irradiated and annealed samples nevertheless show lower microstrain than the annealed unirradiated reference. These results indicate partial relaxation of irradiation-induced lattice defects during annealing, accompanied by enhanced crystallite coarsening at high doses.

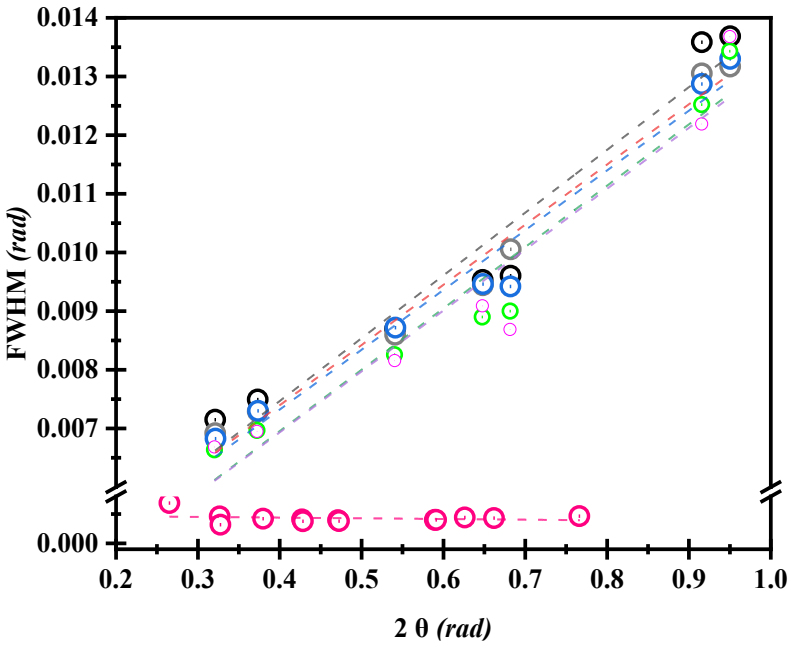


**Fig. 2.** Williamson–Hall analysis of TiN nanoparticles after annealing

The FWHM data points are plotted against 2θ and were transformed according to Eq. (1) for determination of the crystallite size and microstrain. The black open circles and black dashed line represent the annealed initial sample; the gray open circles and red dashed line correspond to 50 kGy; the blue, green, and magenta open circles with their respective dashed fits correspond to 200, 900, and 3500 kGy, respectively. The bright-pink points and dashed line at the bottom represent the instrumental $LaB_6$ standard used to evaluate instrumental broadening.

**3.2. Raman spectra and local lattice dynamics**. The Raman spectrum of the initial powder contains four broad bands centered near 152, 246, 359 and 500 $cm^{-1}$. Their broad shape is consistent with disorder-activated scattering in non-stoichiometric or nanoscale TiN. Studies of TiN films reported acoustic modes in the 216–440 $cm^{-1}$ region and an optical contribution near 570 $cm^{-1}$ [13–15]. The lower frequencies measured here are compatible with weaker effective bonding, nanoscale disorder and the different stress state of free nanoparticles.

Figure 3 compares the Raman spectra of the initial specimen with those irradiated at 50, 200, 900 and 3500 kGy. All four principal bands remain present at every dose, providing no evidence of a radiation-induced vibrational phase transition. Their widths and intensities nevertheless vary with dose. The $\nu_3$ band near 359 $cm^{-1}$ exhibits the clearest positional shift, whereas the modes near 152, 246 and 500 $cm^{-1}$ change more weakly.

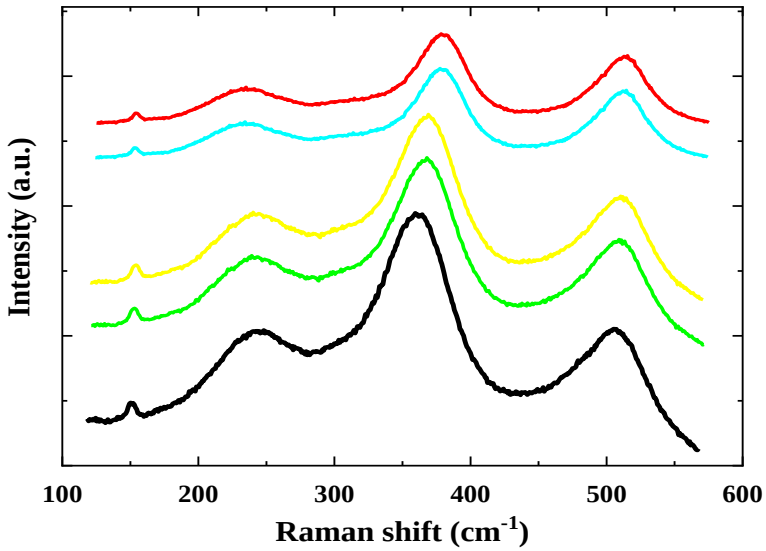


**Fig.3.** Raman spectra of titanium nitride nanoparticles before and after gamma irradiation

For clarity, the spectra are vertically offset and arranged from bottom to top in order of increasing irradiation dose: initial, 50, 200, 900, and 3500 kGy. Analysis of the Raman line-shape parameters shows that the full width at half maximum (FWHM) of $\nu_1$ rises from 5.93 to 7.30 $cm^{-1}$ while its integrated area decreases from 13,375 to 5,045. For $\nu_3$, the FWHM increases from 35.0 to 46.35 $cm^{-1}$ and the area falls from 804,432 to 488,674, consistent with reduced vibrational coherence and increased local disorder. The $\nu_2$ area decreases overall but partially recovers at 3500 kGy relative to 900 kGy. In contrast, the $\nu_4$ area is non-monotonic and increases at the highest dose. The dose response is therefore mode-specific rather than governed by one identical mechanism.

The XRD and Raman findings are therefore complementary. XRD establishes preservation of the long-range cubic framework and reveals reduced post-irradiation oxide formation. Raman data show that gamma exposure still alters the local lattice through defect redistribution, fragmentation of weak bonds and changes in Ti–N interatomic distances. The removal of adsorbed species can densify the near-surface structure, whereas defect creation and recombination modify the distribution of vibrational states [21-25].

**4. Conclusion**. Gamma irradiation at doses up to 3500 kGy preserves the cubic *Fm-3m* framework of TiN nanoparticles. Subsequent annealing at 1173 K produces only a minor rutile $TiO_2$ fraction, and the amount of this oxide decreases from 6.40% to 3.88% as the prior irradiation dose increases. High-dose irradiation followed by annealing promotes crystallite growth to about 50 nm and reduces microstrain and dislocation density. Raman spectra retain four characteristic modes throughout the dose range, while their positions and line-shape parameters change. Therefore, the average crystal structure remains stable even though local bonds, defect populations and surface species evolve. The combined diffraction and vibrational evidence identifies TiN as radiation resistant while showing that gamma exposure can regulate its later oxidation and nanoscale defect state.

**Author Contributions.** A.V.S. (Alena V. Shershneva) conceived and designed the study, performed the formal analysis, conducted the investigation, prepared the original draft of the manuscript, and reviewed and edited the manuscript. M.I. (Mahmoud Ibrahim) contributed to the methodology, validation of the results, data analysis and interpretation, reviewed and edited the manuscript, supervised the research, and approved the final version of the manuscript. All authors have read and agreed to the published version of the manuscript.
**Funding.** Not applicable.
**Data Availability.** The data supporting the findings of this study are available from the corresponding author upon reasonable request.
**Declarations**
**Conflict of Interest.** The authors declare no conflict of interest.
**Competing Interests.** The authors declare that they have no competing interests.
**Ethical Approval.** This article does not involve studies with human participants or animals. Therefore, ethical approval was not required.
**Informed Consent.** Not applicable.
**Acknowledgment.** The authors gratefully acknowledge the support and research facilities provided by Tomsk Polytechnic University, Tomsk, Russian Federation.


## References

[1] Akhtanova, G., Yerlanuly, Y., Parkhomenko, H. P., Solovan, M. V., Mostovyi, A. I., Nurmukhanbetova, A. K., Kireyev, A. V., Danko, I. V., Oreshkin, P. A., Zholdybayev, T. K., Janseitov, D. M., Ramazanov, T. S., & Brus, V. V. (2024). Electron irradiation-induced degradation of TiN thin films on quartz and sapphire substrates. *ACS Omega, 9*(1), 925–933. https://doi.org/10.1021/acsomega.3c07053

[2] Gao, L., Gstöttner, J., Emling, R., et al. (2004). Thermal stability of titanium nitride diffusion barrier films for advanced silver interconnects. *Microelectronic Engineering, 76*(1–4), 76–81. https://doi.org/10.1016/j.mee.2004.07.020

[3] Patsalas, P., Kalfagiannis, N., Kassavetis, S., et al. (2018). Conductive nitrides: Growth principles, optical and electronic properties, and their perspectives in photonics and plasmonics. *Materials Science and Engineering R: Reports, 123*, 1–55. https://doi.org/10.1016/j.mser.2017.11.001

[4] Xue, J. X., Zhang, G. J., Xu, F. F., et al. (2013). Lattice expansion and microstructure evaluation of Ar ion-irradiated titanium nitride. *Nuclear Instruments and Methods in Physics Research Section B: Beam Interactions with Materials and Atoms, 308*, 62–67. https://doi.org/10.1016/j.nimb.2013.05.011

[5] Popović, M., Novaković, M., Mitrić, M., et al. (2017). Xenon implantation effects on the structural and optical properties of reactively sputtered titanium nitride thin films. *Materials Research Bulletin, 91*, 36–41. https://doi.org/10.1016/j.materresbull.2017.03.031

[6] Chen, H. Y., & Lu, F. H. (2005). Oxidation behavior of titanium nitride films. *Journal of Vacuum Science & Technology A, 23*(4), 1006–1009. https://doi.org/10.1116/1.1914815

[7] Arai, Y., & Nakajima, K. (2000). Preparation and characterization of PuN pellets containing ZrN and TiN. *Journal of Nuclear Materials, 281*(2–3), 244–247. https://doi.org/10.1016/S0022-3115(00)00393-7

[8] Fahrenholtz, W. G., Hilmas, G. E., Talmy, I. G., & Zaykoski, J. A. (2007). Refractory diborides of zirconium and hafnium. *Journal of the American Ceramic Society, 90*(5), 1347–1364. https://doi.org/10.1111/j.1551-2916.2007.01583.x

[9] Sutthiruangwong, S., & Mori, G. (2003). Corrosion properties of Co-based cemented carbides in acidic solutions. *International Journal of Refractory Metals and Hard Materials, 21*(3–4), 135–145. https://doi.org/10.1016/S0263-4368(03)00027-1

[10] Mahvash, F., Eissa, S., Bordjiba, T., Tavares, A. C., Szkopek, T., & Siaj, M. (2017). Corrosion resistance of monolayer hexagonal boron nitride on copper. *Scientific Reports, 7*, 42139. https://doi.org/10.1038/srep42139

[11] Morales, H. M., Vieyra, H., Sanchez, D. A., et al. (2024). Synthesis and characterization of titanium nitride–carbon composites and their use in lithium-ion batteries. *Nanomaterials, 14*(7), 624. https://doi.org/10.3390/nano14070624

[12] Christensen, A. N., Romano, V., & Hesse, R. (1975). A neutron diffraction investigation on single crystals of titanium carbide, titanium nitride, and zirconium nitride. *Acta Chemica Scandinavica A, 29A*, 563–568. https://doi.org/10.3891/acta.chem.scand.29a-0563

[13] Saoula, N., Djerourou, S., Yahiaoui, K., et al. (2010). Study of the deposition of Ti/TiN multilayers by magnetron sputtering. *Surface and Interface Analysis, 42*(6–7), 1176–1179. https://doi.org/10.1002/sia.3299

[14] Cheng, Y. H., Tay, B. K., Lau, S. P., et al. (2002). Substrate bias dependence of Raman spectra for TiN films deposited by filtered cathodic vacuum arc. *Journal of Applied Physics, 92*(4), 1845–1849. https://doi.org/10.1063/1.1491588

[15] Ding, Z. H., Yao, B., Qiu, L. X., & Lv, T. Q. (2006). Raman scattering investigation of nanocrystalline δ-$TiN_x$ synthesized by solid-state reaction. *Journal of Alloys and Compounds, 421*(1–2), 247–251. https://doi.org/10.1016/j.jallcom.2005.11.017

[16] Deluca, M., Hu, H., Popov, M. N., et al. (2023). Advantages and developments of Raman spectroscopy for electroceramics. *Communications Materials, 4*, 78. https://doi.org/10.1038/s43246-023-00400-4

[17] Gupta, H., Joshi, K., Gautam, S. K., et al. (2020). Raman scattering from irradiated nanocrystalline zinc oxide thin films: Perspective view on effects of energy loss, ion fluence, and ion flux. *Vacuum, 181*, 109598. https://doi.org/10.1016/j.vacuum.2020.109598

[18] Biradar, S., Chandrashekara, M. N., Manjunatha, Dinkar, A., Devidas, G. B., Bennal, A. S., Rajaramakrishna, R., & Sayyed, M. I. (2024). Synergistic optimization of physical, thermal, structural, mechanical, optical and radiation shielding characteristics in borate glasses doped with $Bi_2O_3$. *Optical Materials, 155*, 115815. https://doi.org/10.1016/j.optmat.2024.115815

[19] Jiang, W., Fu, Q., Wei, H., & Yao, A. (2019). TiN nanoparticles: Synthesis and application as near-infrared photothermal agents for cancer therapy. *Journal of Materials Science, 54*, 5743–5756. https://doi.org/10.1007/s10853-018-03272-z

[20] Cao, L., Zhang, Q., Du, L., et al. (2024). Synthesis and characterization of high-entropy $(TiVNbTaM)_2AlC$ (M = Zr, Hf) ceramics. *Journal of Advanced Ceramics, 13*(2), 237–246. https://doi.org/10.26599/JAC.2024.9220847

[21] Hazem, R., Izerrouken, M., Cheraitia, A., & Djehlane, A. (2019). Raman study of ion beam irradiation damage on nanostructured $TiO_2$ thin film. *Nuclear Instruments and Methods in Physics Research Section B: Beam Interactions with Materials and Atoms, 444*, 62–67. https://doi.org/10.1016/j.nimb.2019.02.011

[22] Rana, A., Sharma, N. K., Bera, S., et al. (2024). Tuning the plasmonic resonance in TiN refractory metal. *Scientific Reports, 14*, 7905. https://doi.org/10.1038/s41598-024-55000-0

[23] Trang, V. T. T., Hang, H. T., Nhi, P. Q., et al. (2024). Enhancement of photothermal conversion by TiN nanoparticles-embedded black paint and applications in solar drying of red chilli. *Materials, 17*(17), 4393. https://doi.org/10.3390/ma17174393

[24] Okrusch, M., Hock, R., Schüssler, U., Brummer, A., Baier, M., & Theisinger, H. (2003). Intergrown niobian rutile phases with Sc- and W-rich ferrocolumbite: An electron-microprobe and Rietveld study. *American Mineralogist, 88*(7), 986–995. https://doi.org/10.2138/am-2003-0706

[25] Dutta, S., Chattopadhyay, S., Sarkar, A., Chakrabarti, M., Sanyal, D., & Jana, D. (2009). Role of defects in tailoring structural, electrical and optical properties of ZnO. *Progress in Materials Science, 54*(1), 89–136. https://doi.org/10.1016/j.pmatsci.2008.07.002